NASA/TM–2001-209621

An Experimental Study of the Ground Transportation System (GTS) Model in the NASA Ames 7- by 10-Ft Wind Tunnel

Bruce L. Storms, James C. Ross, James T. Heineck,
Stephen M. Walker, David M. Driver, Gregory G. Zilliac

Since its founding, NASA has been dedicated to the advancement of aeronautics and space science. The NASA Scientific and Technical Information (STI) Program Office plays a key part in helping NASA maintain this important role.

The NASA STI Program Office is operated by Langley Research Center, the Lead Center for NASA's scientific and technical information. The NASA STI Program Office provides access to the NASA STI Database, the largest collection of aeronautical and space science STI in the world. The Program Office is also NASA's institutional mechanism for disseminating the results of its research and development activities. These results are published by NASA in the NASA STI Report Series, which includes the following report types:

- TECHNICAL PUBLICATION. Reports of completed research or a major significant phase of research that present the results of NASA programs and include extensive data or theoretical analysis. Includes compilations of significant scientific and technical data and information deemed to be of continuing reference value. NASA's counterpart of peer-reviewed formal professional papers but has less stringent limitations on manuscript length and extent of graphic presentations.

- TECHNICAL MEMORANDUM. Scientific and technical findings that are preliminary or of specialized interest, e.g., quick release reports, working papers, and bibliographies that contain minimal annotation. Does not contain extensive analysis.

- CONTRACTOR REPORT. Scientific and technical findings by NASA-sponsored contractors and grantees.

- CONFERENCE PUBLICATION. Collected papers from scientific and technical conferences, symposia, seminars, or other meetings sponsored or cosponsored by NASA.

- SPECIAL PUBLICATION. Scientific, technical, or historical information from NASA programs, projects, and missions, often concerned with subjects having substantial public interest.

- TECHNICAL TRANSLATION. English-language translations of foreign scientific and technical material pertinent to NASA's mission.

Specialized services that complement the STI Program Office's diverse offerings include creating custom thesauri, building customized databases, organizing and publishing research results . . . even providing videos.

For more information about the NASA STI Program Office, see the following:

- Access the NASA STI Program Home Page at *http://www.sti.nasa.gov*

- E-mail your question via the Internet to help@sti.nasa.gov

- Fax your question to the NASA Access Help Desk at (301) 621-0134

- Telephone the NASA Access Help Desk at (301) 621-0390

- Write to:
  NASA Access Help Desk
  NASA Center for AeroSpace Information
  7121 Standard Drive
  Hanover, MD 21076-1320

NASA/TM–2001-209621

An Experimental Study of the Ground Transportation System (GTS) Model in the NASA Ames 7- by 10-Ft Wind Tunnel

Bruce Storms
AerospaceComputing, Inc., Los Altos, California

James C. Ross, James T. Heineck, Stephen M. Walker,
David M. Driver, and Gregory G. Zilliac
Ames Research Center, Moffett Field, California

National Aeronautics and
Space Administration

Ames Research Center
Moffett Field, California 94035-1000

February 2001

Acknowledgments

Available from:

An Experimental Study of the Ground Transportation System (GTS) Model in the NASA Ames 7- by 10-Ft Wind Tunnel

Bruce L. Storms,[*] James C. Ross, James T. Heineck, Stephen M. Walker,

David M. Driver, Gregory G. Zilliac

Abstract

The 1/8-scale Ground Transportation System (GTS) model was studied experimentally in the NASA Ames 7- by 10-Ft Wind Tunnel. Designed for validation of computational fluid dynamics (CFD), the GTS model has a simplified geometry with a cab-over-engine design and no tractor-trailer gap. As a further simplification, all measurements of the GTS model were made without wheels. Aerodynamic boattail plates were also tested on the rear of the trailer to provide a simple geometry modification for computation. The experimental measurements include body-axis drag, surface pressures, surface hot-film anemometry, oil-film interferometry, and 3-D particle image velocimetry (PIV). The wind-averaged drag coefficients with and without boattail plates were 0.225 and 0.277, respectively. PIV measurements behind the model reveal a significant reduction in the wake size due to the flow turning provided by the boattail plates. Hot-film measurements on the side of the cab indicate laminar separation with turbulent reattachment within 0.08 trailer width for zero and ±10 degrees yaw. Oil-film interferometry provided quantitative measurements of skin friction and qualitative oil flow images. The methodology for calculation of the force and pressure coefficients is included to facilitate comparison between computation and experiment. A complete set of the experimental data and the surface definition of the model are included on a CD-ROM for further analysis and comparison.

Nomenclature

a	speed of sound $= \sqrt{\gamma p / \rho}$
c	wind-tunnel contraction ratio
C_D	body-axis drag coefficient $= D / qS$
C_f	skin friction coefficient $= \tau / q$
C_p	pressure coefficient $= (p - p_\infty) / q$
D	body-axis drag
h	trailer height
L_p	pressure level
M	Mach number $= U / a$
OD	outside diameter
p	static pressure
q	dynamic pressure $= \frac{1}{2} \rho U^2$
u	local velocity
Re	Reynolds number $= U*w / v$
S	trailer cross-sectional area $= w * h$
U	free-stream velocity
V	hot-film voltage
w	trailer width
x,y,z	right-handed coordinate system
Ψ	yaw angle (positive nose right)
τ	skin friction
v	kinematic viscosity
ρ	air density

Subscripts

max	maximum value
rms	root mean square
r	settling chamber value
s	static
t	total
w	wall
∞	free-stream value

---

[*] AerospaceComputing, Inc., Moffett Field, California.

Introduction

Because of the enormous size of the U. S. national trucking fleet, a small reduction in fuel consumption equates to a considerable cost savings as well as a reduced environmental impact. For a typical class-8 tractor-trailer, the horsepower required for rolling friction and accessories is greater than that of aerodynamic drag until a highway speed of approximately 50 mph (80 km/hr) (Ref. 1). However, because drag generally varies with the square of velocity, the impact of aerodynamic drag is much more significant at typical highway speeds. At 70 mph (113 km/hr), for example, the power required to overcome aerodynamic drag is 65% of the total fuel consumption. It is estimated that a 25% reduction in aerodynamic drag would yield a 10–15% reduction in fuel consumption (Ref. 2). This savings is considerably greater than the estimated possible savings of other technology improvements, such as improved engine efficiency and weight reduction.

The trucking industry currently relies on wind-tunnel testing and field experiments for aerodynamic design and analysis. However, this process is costly due to the expenses for both detailed scale models and wind-tunnel occupancy. The use of CFD analysis could significantly reduce the cost of aerodynamic design by reducing the number of models tested in the near term and eventually replacing most wind-tunnel testing in the future. This experimental study is part of a multi-year program focused on the development of a validated aerodynamic simulation capability for tractor-trailer configurations. The specific goal of this experiment is to provide high-quality aerodynamic data for direct validation of computational tools being developed by national labs, academia, and industry.

A previous experimental study of the GTS model was conducted in the Texas A&M University (TAMU) Low-Speed Wind Tunnel (Ref. 3). This facility has a 7-ft x 10-ft (2.13-m x 3.05-m) test section similar to that used in the current study except that the corners have 1-ft (0.305-m) fillets that house lamps for photographic lighting. The 1/8-scale GTS model was tested at a Reynolds number of 1.6 million based on trailer width of 12.75 in (32.38 cm). The measurements included surface pressures, forces and moments, oil flow, tufts, smoke, and wake measurements with a 7-hole probe and a tufted grid. For the GTS model configuration without wheels, the body-axis drag coefficients at zero yaw and wind averaged were 0.246 and 0.266, respectively. Data were also obtained for five add-on drag reduction devices consisting of two ogival boattails and three slants similar to those used by Ahmed et al (Ref. 4). For the configuration without wheels, the largest overall drag reduction (wind averaged) of 10.1% was obtained by the 8-ft ogive configuration.

The effectiveness of aerodynamic boattail plates was investigated on a full-scale tractor-trailer configuration in the 80- by 120-Foot Wind Tunnel at NASA Ames Research Center in 1988 (Ref. 5). The boattail plates consist of four panels that are mounted perpendicular to the aft-facing trailer door. Typically, the plates are inset from the edges of the trailer on three sides and mounted flush with the trailer edge on the bottom. This passive device traps recirculating flow between the plates and the rear corners of the trailer. As a result, the flow separating from the rear of the trailer is turned inward slightly. This yields an increase in the base pressure and a reduction in the overall drag. The optimum boattail plate configuration reduced the overall drag by about 10% at zero yaw angle. Relative to the baseline configuration (without plates), measurements indicated that the base pressure between the boattail plates was significantly increased whereas the pressure between the plates and the edge of the trailer was reduced. Unsteady pressure measurements were also made for pressure taps at the center of the trailer rear panel. A consistent peak was observed between 1.8 and 2.0 Hz both with and without boattail plates. This frequency corresponds to a Strouhal number of 0.12 based on trailer width. The only significant and repeatable effect of the boattail plates was an increase in the high-frequency content of the fluctuating pressure.

The goal of the present study was to provide high-quality experimental data on a simplified tractor-trailer geometry for CFD validation. In addition to the force, moment, and pressure measurements made in the TAMU test, additional on-body and off-body details were provided by hot-film anemometry, oil-film interferometry, and particle image velocimetry. Measurements were made at various yaw angles to study the influence of crosswind and at various wind speeds to determine the effect of Reynolds number. An additional configuration was tested with aerodynamic boattail plates to provide a simple geometry modification for CFD simulation. The entire data set has been archived on CD-ROM for easy reference.

Experimental Setup

The experiment was conducted in the 7- by 10-Foot Wind Tunnel #1 operated by the Army in cooperation with the NASA Ames Research Center. This atmospheric facility is a closed-circuit wind tunnel incorporating a 15-ft (4.57-m) long test section with a constant height of 7 feet (2.13 m) and a nominal width of 10 feet (3.05 m) with a 1% wall divergence. The boundary layer thickness at the test section entrance is 2.1 in (5.3 cm), which corresponds to a displacement thickness of 0.6 in (1.5 cm). The boundary layer profile resembles that of a turbulent flat plate described by the $1/7^{th}$-power law (Ref. 6) and is included on the CD-ROM. The multiple turbulence-reducing screens in the circuit yield empty test-section turbulence intensities in the longitudinal, lateral, and vertical directions of 0.1%, 0.3%, and 0.3%, respectively, for a test condition of M = 0.22. These turbulence levels correspond to an RMS turbulence intensity of 0.25% and a turbulence factor of 1.2.

The baseline geometry for this investigation is the GTS model without wheels, which is representative of a generic 1/8-scale class-8 tractor-trailer geometry with a cab-over-engine design. Designed for CFD validation, this geometry includes a simple tractor design and no tractor-trailer gap, which facilitates grid generation and avoids the associated flow complexities. The model was fabricated and tested at Texas A&M University and subsequently loaned to NASA Ames for further study. All flat model surfaces are aluminum sheet metal, and all curved surfaces were machined from Ren Shape 450. Figure 1 shows the GTS model installed in the NASA Ames 7- by 10-Ft Wind Tunnel. Figure 2 shows the GTS model dimensions non-dimensionalized by the trailer width of 12.75 in (32.38 cm). Note that all data presented in the current study were obtained without wheels. The model was instrumented with 79 pressure taps, as shown in Figure 2. A tabular list of the tap locations is included in Ref. 3 and on the CD-ROM.

Because of the model length and the interest in wake details, the GTS model was located at a position 5.25 in (13.33 cm) downstream of the beginning of the test section, as shown in Figures 3–4. Mounted level in the test section, the bottom of the model was located 3.0 in (7.6 cm) above the wind-tunnel floor. Four cylindrical struts connected the model to the scale system, and 1.5-in (3.8-cm) diameter cylindrical

fairings (non-metric) extended from the floor to within 0.25 in (0.63 cm) of the bottom of the model.

As a simple geometry modification for computations, aerodynamic boattail plates were provided by Continuum Dynamics, Inc. A photograph of the boattail plates installed on the rear of the trailer is shown in Figure 5. The plates extended 3.75 in (9.52 cm) from the end of the trailer and were inset from the sides and top of the trailer by 0.625 in (1.59 cm). The bottom plate was mounted flush with the bottom of the trailer.

The installation side view (Figure 4) also shows the location of the three rows of pressure taps mounted flush with the right test-section wall (looking upstream). For ease of comparison with CFD, the test-section static pressure was obtained from a single wall-pressure tap located at x/w = 4.5, y/w = 2.6, and z/w = -4.7, as shown in Figure 4. This wall-pressure, p_{sw}, was used to calculate pressure coefficients as follows:

$$C_p = \frac{p - p_{sw}}{q_\infty},$$

where the tunnel dynamic pressure, q_∞, was calculated as the difference between the settling-chamber static pressure (p_r) and the reference wall tap static pressure (p_{sw}). A correction for the difference between the settling-chamber total and static pressure was included as follows:

$$q_\infty = p_t - p_{s\infty} = \frac{c^2}{c^2 - 1}(p_r - p_{sw}).$$

The contraction ratio, c, is the ratio of the cross-sectional area of the settling chamber (upstream of the contraction) to that of the test section (c = 14.14 for the NASA Ames 7- by 10-Ft Wind Tunnel). The surface pressures were measured with an electronically scanned pressure system, and time averaging provided an uncertainty in the calculated pressure coefficients of ±0.002.

The model was mounted on the facility scale system, which includes a turntable for remote model positioning. Because the facility scales measure wind-axis forces (parallel and perpendicular to the axis of the wind tunnel), a coordinate transformation was employed to determine the body-axis drag (the force along the longitudinal axis of the model). The drag

measurements are accurate to within ±1 lb (4.45 N). The repeatability of the drag coefficient measurements was ±0.001 for $\Psi \geq -5$ degrees and ±0.01 for $\Psi <$ −5 degrees. These error bands include both measurement resolution and point-to-point repeatability. All drag measurements are reported in the body-axis coordinate system. Due to erroneous readings in the lift measurements, no lift, pitching moment, or rolling moment data are presented. In addition, no sideforce or yawing-moment data are presented, but these data are available on the CD-ROM for further analysis.

Using the variation of drag with yaw angle, wind-averaged drag coefficients were computed using the SAE Recommended Practice of Ref. 7. This practice assumes that the mean wind speed in the United States of 7 mph (11.2 km/hr) has an equal probability of approaching the vehicle from any direction. This mean wind speed and the vehicle velocity were used to calculate a weighted average of the drag coefficient at various yaw angles. The wind-averaged drag coefficients reported in this paper were computed for a typical highway speed of 55 mph (88 km/hr).

Force and pressure measurements were made at yaw angles ranging from −14 to 14 degrees in 2.5-degree increments between ±12.5 degrees. A majority of the results that follow focus on yaw angles of 0, 10, and −10 degrees. Detailed data sets were obtained at Reynolds numbers of 2 million and 740,000, which correspond to wind-tunnel velocities of 205 mph and 75 mph, respectively (full-scale Reynolds numbers vary from 4 to 6 million). The high-velocity condition was chosen to maximize Reynolds number while avoiding compressibility effects. The low-velocity condition was chosen to minimize compressibility effects for incompressible computational algorithms. In addition, a Reynolds-number variation study was conducted at zero yaw for Re = 300,000 to 2 million. Hot-film anemometry, oil-film interferometry, and particle image velocimetry were conducted at limited yaw angles and tunnel speeds.

Results and Discussion

The results that follow do not include any corrections for wind-tunnel wall effects. Therefore, only computational grids that include the tunnel walls will yield comparable results. Also, the computations must use the same static pressure reference (detailed above) for comparison with the experimental force and pressure measurements.

I. Drag Measurements

The variation of the body-axis drag coefficient with yaw angle for the model with and without boattail plates is presented in Figure 6. Because of the poor repeatability for yaw angles less than −5 degrees, only data for positive yaw angles are shown. The poor repeatability at negative yaw angles is due to facility scale issues and is not an indication of flow irregularities. The zero-yaw value of drag agrees well with the results from Ref. 3, but the increase in drag with yaw angle is larger than that of the previous measurements. The differences between the current results and those presented in Ref. 3 can be attributed to the location of the static pressure reference used to calculate tunnel dynamic pressure. These differences are also evident in the static pressure measurements given in the next section.

Relative to the GTS baseline configuration, the addition of boattail plates yields an average of 20% reduction in drag for yaw angles from zero to 14 degrees. The wind-averaged drag coefficients were calculated using the data at non-negative yaw angles and assuming symmetry of the drag curves about zero degrees. The resulting wind-averaged coefficients with and without boattail plates are 0.225 and 0.277, respectively, which correspond to a 19% reduction in drag. This reduction is almost twice that measured in the full-scale test (Ref. 5) because of simplified geometry of the GTS model (i.e., no wheels, no gap, no mirrors, cab-over design, etc.). The drag reduction from the boattail plates is also almost double that measured with the best add-on device of Ref. 3 (8-ft ogival boattail). This may be due to the effects of the stagnation point where the flow reattaches to the boattail plates. The local stagnation point on the boattail plates provides more flow turning than is possible from an aerodynamically contoured afterbody.

The variation of the drag coefficient with Reynolds number is presented in Figure 7 for a yaw angle of zero degrees. The Reynolds number was first varied from 300,000 to 2 million with increments of 100,000 and then reduced to 300,000 in larger increments to check data repeatability. The differences in the two curves at the lower Reynolds numbers represent the uncertainty in the data due to the facility scale system resolution as well as possible mechanical and/or aerodynamic hysteresis. Note that

4

there is a significant variation in the drag coefficient for Reynolds numbers below 1 million. Above this value, the Reynolds-number effect is minimal. The variation of the average base pressure coefficient on the trailer door is less than 0.005 for the same Reynolds-number range. This suggests that the significant increase in drag coefficient at Reynolds numbers below 1 million must be due to flow variations around the front of the model. Because flow separation from the aft of a bluff body is relatively insensitive to Reynolds number, the results obtained for Reynolds numbers above 1 million are expected to be representative of the full-scale flowfield (Re = 4–6 million).

II. Surface Pressures

Seventy-nine surface pressures were located on the model, and 43 additional surface pressures were located on the right wall of the test section (looking upstream). In addition, one unsteady pressure transducer was located on the rear of the trailer. Pressure coefficients were calculated using a selected wall pressure as the test-section static pressure (as detailed above). By using the same static pressure reference in the CFD simulations, a direct comparison can be made between experiment and computation. However, it should be noted that the selected wall pressure varies with yaw angle, as shown in Figure 8, due to the position of the model relative to the reference pressure tap. Because of this variation, the surface pressures on the model symmetry plane do not agree at corresponding positive and negative yaw angles.

Horizontal-Plane Surface Pressures: A longitudinal row of pressure taps was located at half trailer height (y/w = 0.696) on the left side of the model. The variation of the horizontal plane pressures with yaw angle is presented in Figure 9 for the baseline configuration (no boattail plates). The tap at x/w = 0 is on the front of the tractor and indicates a pressure near stagnation, as expected. There is a suction peak as the flow negotiates the corner, and then the pressure is relatively constant until near the end of the trailer. At this point, the flow again accelerates due to the converging streamlines after flow separation from the aft of the trailer. The effect of boattail plates at zero yaw (Figure 10) is to reduce the pressures near the end of the trailer because of the increased flow curvature in the wake.

Top Surface Pressures: Another longitudinal row of pressure taps was located along

the model centerline (z/w = 0) on the top of the model (y/w = 1.392). The effect of the model surface curvature above the cab is seen as a suction peak of about C_p = -0.4 in Figure 11. Further aft, the pressure is relatively constant until near the end of the trailer, where the flow is accelerated due to the same effect noted for the horizontal surface pressures. The reduced pressures for the non-zero yaw angles correspond to higher-velocity flow over the top of the truck. This velocity increase is due to the increase in projected area of the truck with increasing yaw angle. The asymmetry between the +10- and –10-degree yaw angles is due to the variation of the reference wall pressure, as detailed above. Again, the effect of the boattail plates at zero yaw (Figure 12) is to reduce the pressure near the end of the trailer.

Symmetry-Plane Surface Pressures: All the pressures along the symmetry plane (z/w = 0) are presented in Figure 13 as a function of vertical location. This format gives an indication of the drag, which is related to the pressure difference between the front and aft of the model. The pressure distribution at 10 degrees yaw reveals increased suction on the rear of the trailer relative to the zero-degree case. This increased suction corresponds to an increase in drag for non-zero yaw angles. Figure 14 presents the effect of boattail plates on the symmetry plane pressures at zero yaw. The effect of the boattail plates is evident only on the lower portion of the rear of the trailer where the pressures are significantly increased. This increased base pressure with boattail plates corresponds to the reduction in drag noted above.

Base Surface Pressures: In addition to the row of surface pressures along the symmetry plane, two other vertical rows of surface pressures were located on the back of the trailer at z/w = 0.22 and 0.44. The base pressure variation with lateral position is presented in Figure 15 for yaw angles of zero and ±10 degrees. The zero-yaw measurements indicate little variation in base pressure with lateral position. A greater variation in the base pressures is observed at a yaw angle of 10 degrees. With taps on the windward side of the trailer, the base pressures are lower than at zero yaw and the pressure increases with increasing lateral distance from the symmetry plane. At –10 degrees yaw, the pressure taps are on the leeward side of the trailer and the base pressures on the upper portion of the trailer are less than those on the windward side. The effect of boattail plates on the base pressures at zero yaw is presented in Figure 16. As noted above, the boattail plates significantly increase the base pressure on the lower portion on the

rear of the trailer. Similar to the baseline config-
uration at zero yaw, there is little variation in the
boattail-case base pressures with lateral position.

The effect of Reynolds-number variation on the
trailer base pressures is presented in Figures 17–18.
Although the variation of the average base pressure
coefficients (Figure 17) is small (less than 0.005 for
$350,000 \leq Re \leq 2$ million), there is an obvious break
in the curve at 1 million. At Reynolds numbers
below 1 million, the reduced back pressure (increased
suction) on the trailer corresponds to the increased
drag measured for the same range (Figure 7).
However, the small change in base pressures (less
than 2%) is not sufficient to account for the 60%
difference in drag between Reynolds numbers of 1
million and 350,000. As mentioned previously, this
suggests that there must be significant Reynolds-
number effects on the forebody flowfield. Figure 18
shows that the base pressure distribution is also
significantly affected by variations in Reynolds
number. In particular, the vertical pressure
distributions are more symmetrical at the lower
Reynolds number. This is likely due to the thicker
boundary layer at lower Reynolds numbers and its
effect on the flow underneath the truck. As with the
data for $Re = 2$ million (Figure 15), there is little
variation in the pressure distributions with lateral
position for $Re = 740,000$.

Test-Section Wall Pressures: Two
horizontal rows and one vertical row of pressure taps
were installed in the north test-section wall ($z/w =$
-4.7), as illustrated in the installation drawing
(Figure 4). The pressure distributions measured at
yaw angles of 0, 10, and -10 degrees are presented for
each of these rows in Figures 19–21. As detailed
above, the wall tap at $x/w = 4.5$ and $y/w = 2.6$ was
chosen as the freestream static pressure for calculation
of pressure coefficients. This results in a pressure
coefficient of exactly zero for the chosen wall tap
which is included in Figure 19. Some of the scatter
observed in the wall pressures may be due to
imperfections in the pressure-tap installation or wall-
panel construction.

Unsteady Base Pressure: A single unsteady
pressure transducer was installed flush with the aft-
facing panel near the right side at $y/w = 0.63$ and z/w
$= -0.46$. The signal was sampled at 1500 Hz for 210
seconds with anti-aliasing filters at 750 Hz. A sample
time series is presented in Figure 22, where some
signal periodicity is evident. Spectra for various
configurations are presented in Figures 23–26 for

frequencies below 150 Hz. The spectra at higher
frequencies are relatively featureless and therefore are
not presented. In general, the signal is broadband with
no obvious peaks from periodic shedding that might
be expected from a bluff body. Figure 23 shows that
the spectrum does not vary appreciably between zero
and 10 degrees yaw. At -10 degrees, however, the
spectrum of the sensor near the windward edge is
5–10-dB higher than at zero yaw (Figure 24). Figure
25 shows that the effect of boattail plates is to reduce
the level for frequencies below 90 Hz.

The effect of Reynolds number variation on the
fluctuating pressure spectra is presented in Figure 26.
Unlike the relatively broadband spectrum for $Re = 2$
million, the spectrum for $Re = 740,000$ includes a
distinct peak at approximately 9 Hz. Using velocity
scaling, a corresponding local maximum at 24 Hz can
also be identified in the spectrum for $Re = 2$ million.
These peaks correspond to a Strouhal number of
0.085 based on trailer width. This Strouhal number is
of the same order as that measured at full scale (Ref.
5) and is indicative of relatively organized shedding.

III. Oil-Film Interferometry (OFI)

The OFI technique is based on the principle that
oil on a surface, when subjected to shear, will thin at
a rate related to the magnitude of the shear. The
measurement of skin friction involves measuring the
oil-thickness distribution, recording a history of the
tunnel run conditions, and knowing the properties of
the oil. The oil film's thickness distribution is
determined from the interference patterns that can be
seen in the oil as a result of interference between
reflected light from the model surface and the reflected
light from the air-oil interface. The spacing of the
dark bands (or fringes) is a measure of the slope of the
oil front, and the fringes are contours of constant oil
thickness. The uncertainty of this technique is $\pm 5\%$;
more details can be found in Ref. 8.

OFI measurements were made on the top and
right side of the GTS model without boattail plates.
An image of the fringe patterns observed on top of
the trailer is shown in Figure 27 for 10 degrees yaw.
In addition to the fringe patterns, the oil flow shows
the effect of the vortex that forms from the flow off
the windward side of the model. The vortex path is
also evident in the vector plot of skin friction
presented in Figure 28 for 10 degrees yaw. The
relatively short vectors in the first two rows indicate
laminar flow on the front of the model where the flow
accelerates along the curved surface. Transition to

6

turbulence occurs near x/w = 1.0, as indicated by the higher skin-friction values in that region. The vortex path extends inboard from the left side of the model aft of about x/w = 2.0.

A plot of the skin-friction magnitude along the centerline on top of the model is presented in Figure 29 for zero yaw. Also included in the figure is the theoretical curve for skin friction on a turbulent flat plate. Because of the shape of the front of the GTS model, the boundary layer is laminar until near the end of the surface curvature. As a result, the skin friction is initially significantly less than that of the turbulent flat plate. The skin friction peaks during transition, after which it approximates the theoretical curve for a turbulent boundary layer. Quantitative results are also available for the skin friction on the right side of the model at zero and 10 degrees yaw (included on CD-ROM).

The OFI measurements were made only at a Reynolds number of 2 million. At lower Reynolds numbers, the skin-friction distribution on the top of the model is expected to be very similar except for the location of boundary-layer transition. As the Reynolds number is reduced, laminar-to-turbulent transition will be delayed and the peak in the skin friction distribution (Figure 29) will move aft. At Reynolds numbers below 1 million, it is expected that OFI would show a significant separation region on the side of the tractor that would account for the corresponding increase in drag coefficient.

IV. Hot-Film Anemometry

Similar to hot-wire anemometry, the hot-film technique is based on the principle that a change in temperature affects the current flow or voltage drop through a fine metallic connection. For hot-film anemometry, a thin metallic substrate, or "film," is mounted flush with the surface of interest and is heated electrically by a circuit that maintains either constant current or constant voltage drop. When air flows over the hot film, the cooling, which is a function of the skin friction, can be detected as variations in voltage (for constant current) or current (for constant voltage).

Hot-film measurements were made on the right side of the cab to determine the existence and extent of flow separation in the vicinity of the front corner radius. Mylar sheets with an array of hot-film sensors were mounted to the side of the cab as shown in Figure 30. Sixteen sensors were measured simultaneously at 1024 Hz for 2 seconds. Several sensor configurations were studied, but the results that follow are for streamwise rows of hot-film sensors located at y/w = 0.35 and 0.64 with clustering near the corner radius. The hot-film sheets and measurement system were provided by Tao of Systems Integration, Inc., with funding from the NASA Small Business Innovative Research (SBIR) program. Further details can be found in the SBIR Phase II final report (Ref. 9).

Spectra of four hot-film sensors (#2, 3, 4, & 5) on the corner radius at y/w = 0.35 are presented in Figures 31–32. In general, the spectra are relatively flat and devoid of obvious peaks, which suggests that there is no extensive separation region. If separation were present, periodic flow oscillations would likely result in significant peaks in the spectra of sensors near the separation region. At zero yaw (Figure 31), the spectra for the first three sensors are at the same level whereas the fourth sensor is 20 dB higher. This is indicative of laminar-to-turbulent transition of the boundary layer. At 10 degrees (Figure 32), only the first two sensors are at the lower (laminar) level, so the boundary layer transitions earlier than at zero yaw.

Spectra of three hot-film sensors near the corner radius at y/w = 0.64 are presented in Figures 33–34 for 10 degrees yaw. At this height on the model, only the first sensor, at x/w = 0.06, indicates laminar flow (Figure 33). All subsequent sensors in the streamwise row are at a higher level, which implies that boundary-layer transition occurs between the first and second sensors. Figure 34 presents a comparison of the spectra for Reynolds numbers of 2 million and 740,000. At the lower velocity, there is a significant increase in the spectra below 100 Hz. This is indicative of large-scale flow unsteadiness in a separation region. The remaining sensors in the streamwise row are all at a level similar to that of the sensor at x/w = 0.09. This low-frequency peak is evident for Reynolds numbers less than 1 million and corresponds with the Reynolds-number effect observed in the pressure and drag measurements.

The statistics of all 16 hot-film sensors at y/w = 0.35 are presented in Figure 35 for yaw angles of 0, 10, and –10 degrees. The top plot shows the mean value of the hot-film signal, which is proportional to the third power of surface shear stress (Ref. 9). A drop in the mean signal level occurs at all bifurcation points (i.e., flow separation, reattachment, stagnation). The plots of RMS and intermittency give

an indication of the state of the boundary layer. The lower plot shows the positions of the sensors relative to the 1.1-in. (2.85-cm) corner radius at the front of the cab. As indicated in the figure, the first sensor was located on the front of the cab, the next three were on the corner radius, and the remaining sensors were on the side of the truck.

At all yaw angles, the mean voltage level initially increases up to sensor #3 as the flow accelerates around the corner radius. The subsequent drop in the mean voltage at sensor #4 indicates flow separation. The RMS and intermittency levels show that the boundary layer is laminar at sensor #3 for all yaw angles. The increase in RMS and intermittency at sensor #4 for the 10-degree case indicates transition to turbulence in advance of the other yaw angles. This is to be expected due to the adverse pressure gradient on the leeward side of the model. The mean, RMS, and intermittency levels peak at or before sensor #5, indicating laminar-to-turbulent transition in the separated shear layer. All levels subsequently drop at sensor #6 after flow reattachment. In summary, a relatively small (0.08w) laminar separation bubble is found at all three yaw angles. The extent of this separation region on the leeward side is no larger than that of the windward side, contrary to what was expected. Oil-film interferometry measurements on the side of the model (not shown) corroborate these results.

V. Particle Image Velocimetry (PIV)

PIV measures fluid velocities by time-sequential imaging of the displacement of individual tracer particles in the flow. A pulsed-laser light sheet illuminates the tracer particles, or seed, and a correlation of two successive images yields the distance and direction that the particles move. For 2-D velocity measurements, a single camera oriented normal to the light sheet measures the motion of the tracer particles in a plane. To obtain three components of velocity, two cameras view the identical region of interest obliquely and simultaneously. By viewing the laser light sheet obliquely, both cameras can record the movement of the particles through the light sheet. This method exploits the difference in perspective between the two cameras and derives the third component of velocity mathematically. More details on this PIV method can be found in Ref. 10.

Three-component PIV was conducted for several measurement plane orientations, as shown in Figure 36. For each orientation, the laser light sheet was moved to several locations in the trailer wake. Measurements were made with and without boattail plates for most locations. A summary of the locations, yaw angles, and tunnel conditions is presented in the table.

A sample of the horizontal plane measurements at half height is presented in Figure 37. This figure includes three components of velocity in the trailer wake with and without boattail plates. The upper figures present contours of the streamwise velocity component, which reveal that the size of the wake is significantly reduced by the presence of the boattail plates. At the streamwise location of $x/w = 8.6$, for example, the addition of the boattail plates reduced the width of the wake by 16% (from 0.94w to 0.79w). The lower figures present in-plane velocity vectors that are colored by the magnitude of the out-of-plane velocity. As in the streamwise velocity contours, these figures illustrate that the boattail plates produce a narrowing of the wake, which leads to increased base pressure and reduced drag.

Orientation	Location	Yaw, deg.	Re / 10^6
Horizontal	y/w = 0.35, 0.70, 1.05	0, 10	2.0, 0.74, 0.3*
Cross-stream	x/w = 8.0, 8.35, 8.78	0, 10	2.0, 0.74
Streamwise	z/w = 0, 0.25**	0	2.0*, 0.74*

* without boattail plates only

** measured at –4-deg. yaw

Summary

Experimental measurements were obtained for CFD validation of a simplified 1/8-scale tractor-trailer configuration. To reduce complexity of the geometry and resulting flowfield, the model design included a cab-over-engine design, no tractor-trailer gap, and no wheels. Add-on boattail plates were also tested on the rear of the trailer to provide a simple drag-reduction device for computation. The boattail plates provided a 19% reduction in wind-averaged drag and reduced the size of the wake by turning the flow downstream of the trailer. Particle image velocimetry measurements provide details of the off-body flowfield in the model wake. Hot-film measurements on the side of the model revealed a laminar separation bubble in the vicinity of the corner radius. Oil-film interferometry yielded quantitative measurements of skin friction and qualitative surface flow visualization. Due to differences in the static-pressure reference, there were some discrepancies between the current results and measurements from a previous test of the same model. To facilitate comparison to computation, the methodology is provided for calculation of the force and pressure coefficients. If not included with the hardcopy of this report, a CD-ROM data archive is available for further study.

Future Work

A follow-on wind-tunnel experiment will include a conventional cab-behind-engine tractor design and a tractor-trailer gap. The gap flow and the effect of tractor side extenders will be studied in detail in the NASA Ames 7- by 10-Ft Wind Tunnel. Although this report shows little variation of drag for Re > 1 million, the conventional tractor design and the tractor-trailer gap are expected to produce results with significant Reynolds-number sensitivity. To document this sensitivity up to full-scale Reynolds numbers (4–6 million), the same model will later be tested in the Ames 12-Ft Pressure

References

[1] McCallen R., Couch, R., Hsu, J., Leonard, A., Brady, M., Brownad, F., Hammache, M., Salari, K., Rutledge, W., Ross, J., Storms, B., Heineck, J.T., Driver, D., Bell, J., Zilliac, G., Progress in Reducing Aerodynamic Drag for Higher Efficiency of Heavy Duty Trucks (Class 7-8), 1999-01-2238, Gov/Industry Meeting, Washington, D.C., April 26–28, 1999.

[2] McCallen R., Flowers, D., Dunn, T., Owens, J., Leonard, A., Brady, M., Brownad, F., Hammache, M., Salari, K., Rutledge, W., Ross, J., Storms, B., Heineck, J.T., Driver, D., Bell, J., Zilliac, G., Walker, S., Aerodynamic Drag of Heavy Vehicles (Class 7–8): Simulation and Benchmarking, 2000-01-2209, SAE Gov/Industry Meeting, Washington, D.C., June 19–21, 2000.

[3] Croll, R. H., Gutierrez, W. T., Hassan, B., Suazo, J. E., and Riggins, A. J., "Experimental Investigation of the Ground Transportation Systems (GTS) Project for Heavy Vehicle Drag Reduction," SAE Paper 960907, February 1996.

[4] Ahmed, S. R., Ramm, G., and Faltin, G., "Some Salient Features of the Time-Averaged Ground Vehicle Wake," SAE Paper 840300, 1984.

[5] Lanser, J. M., Ross, J. C., and Kaufman, A. E., "Aerodynamic Performance of a Drag Reduction Device on a Full-Scale Tractor/Trailer," SAE Paper 912125, September 1991.

[6] Schlichting, H., *Boundary-Layer Theory*, Seventh Edition, McGraw-Hill, New York, 1979, pp. 636–640.

[7] "SAE Wind Tunnel Test Procedure for Trucks and Buses," SAE J1252 JUL81, SAE Recommended Practice, July 1981.

[8] Driver, D. M., "Application of Oil Film Interferometry Skin-Friction to Large Wind Tunnels," AGARD CP-601, Paper no. 25, 1997.

[9] Tao of Systems Integration, Inc., "Interactive Flow Measurement (IFM) System for High-Reynolds Number Wind-Tunnel Testing," NASA SBIR Phase II Final Report, Contract Number NAS2-97007, March 1999.

[10] Heineck, J. T., and Walker, S. M., "3D PIV in Wind Tunnel Applications: Measurements of a Truck Wake," SAE Paper 199-01-5600, October 1999.
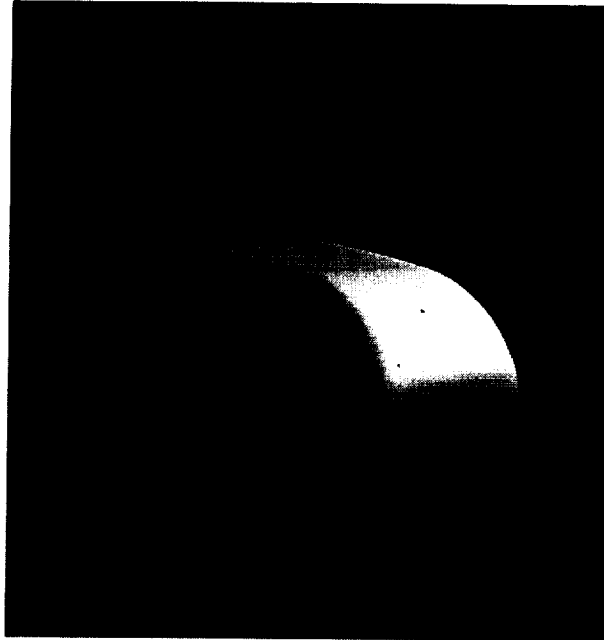
Figure 1: GTS model installed in the NASA Ames 7- by 10-Ft Wind Tunnel.
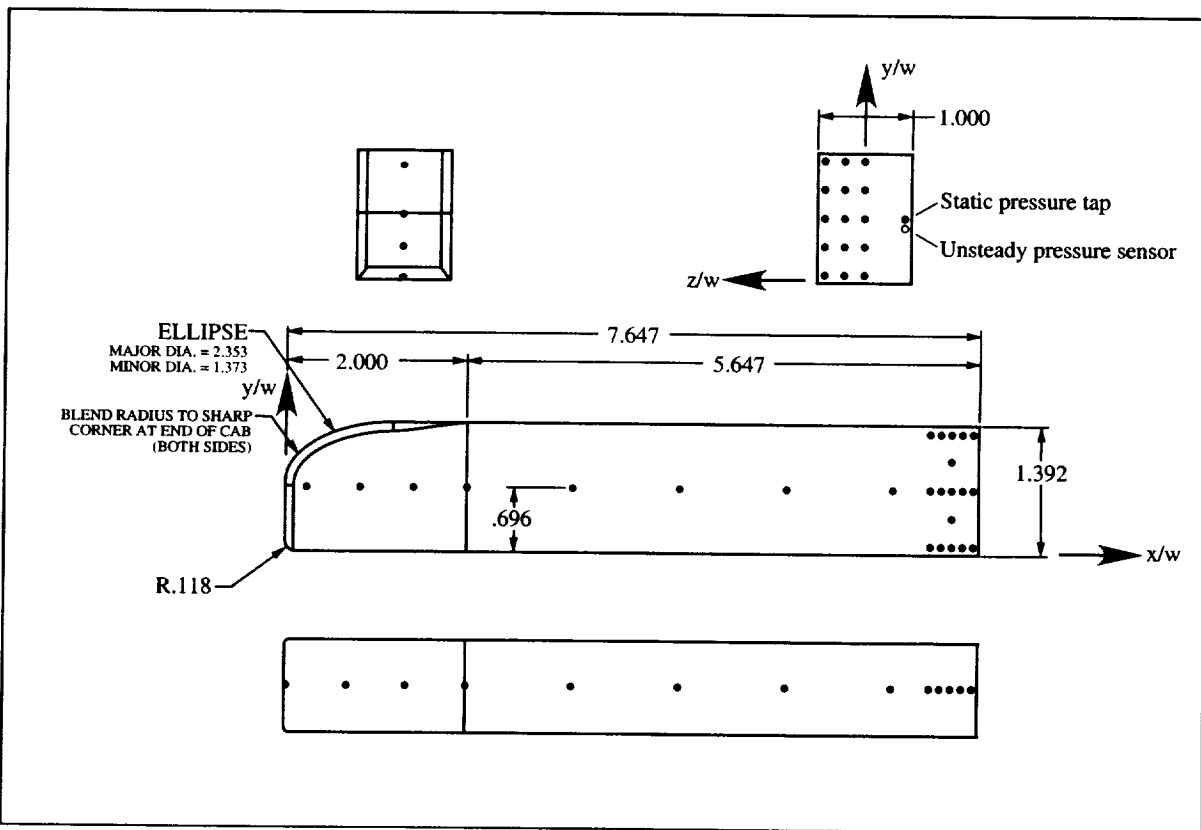
Figure 2: GTS geometry and pressure tap locations. All measurements non-dimensionalized by trailer width, w = 12.75 in (32.38 cm).
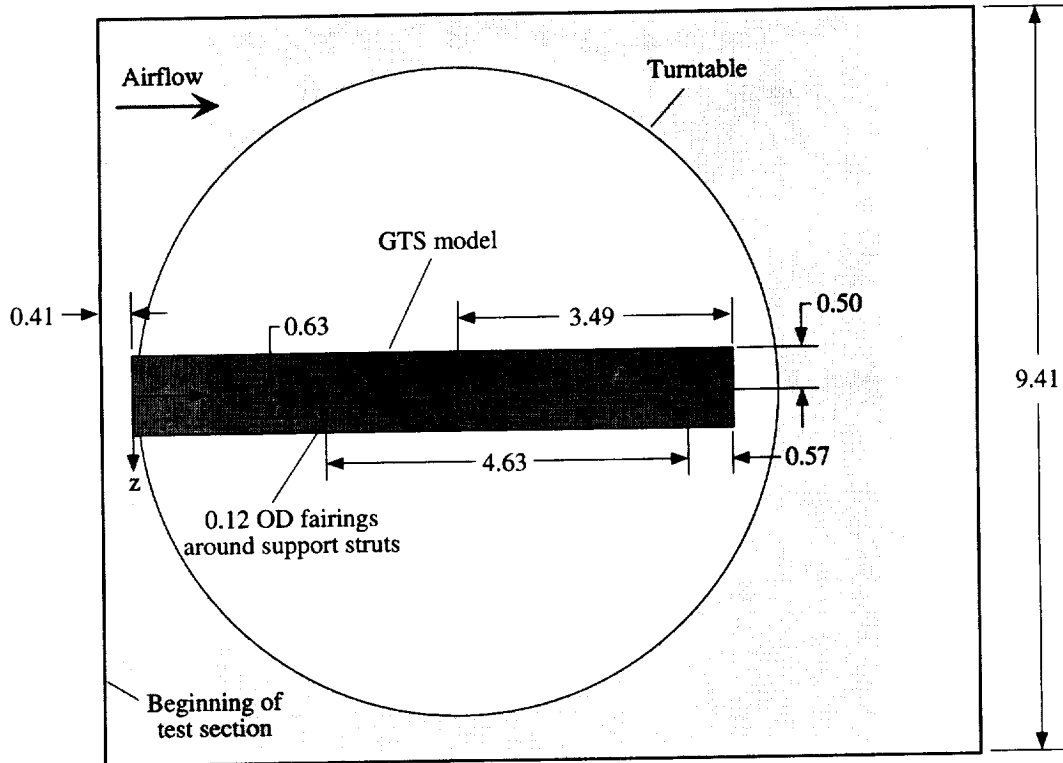
Figure 3: GTS model installation, top view. All measurements non-dimensionalized by trailer width, w = 12.75 in (32.38 cm).
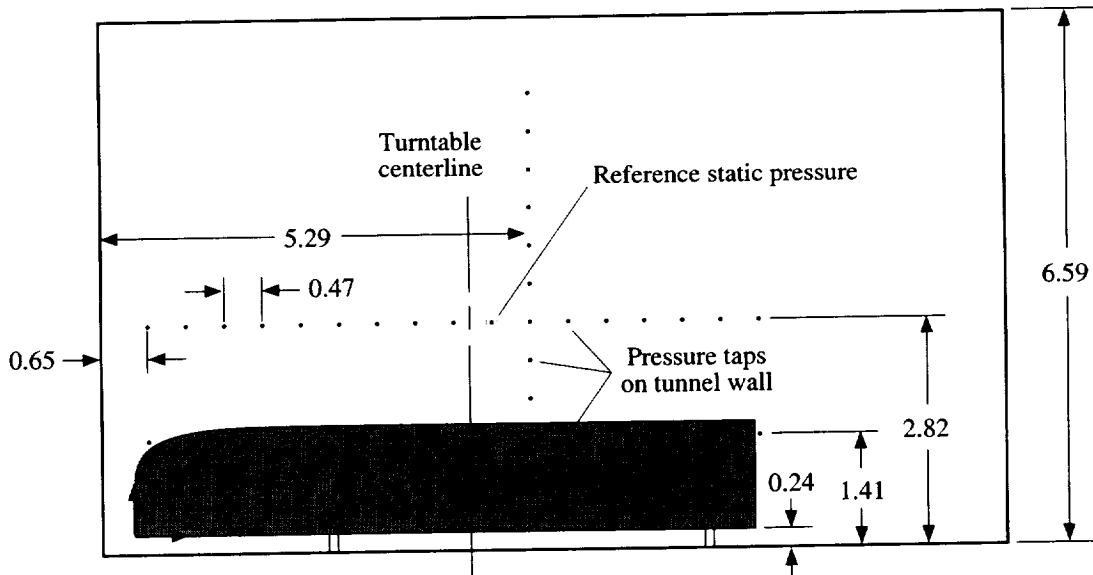
Figure 4: GTS model installation, side view. All measurements non-dimensionalized by trailer width, w = 12.75 in (32.38 cm).
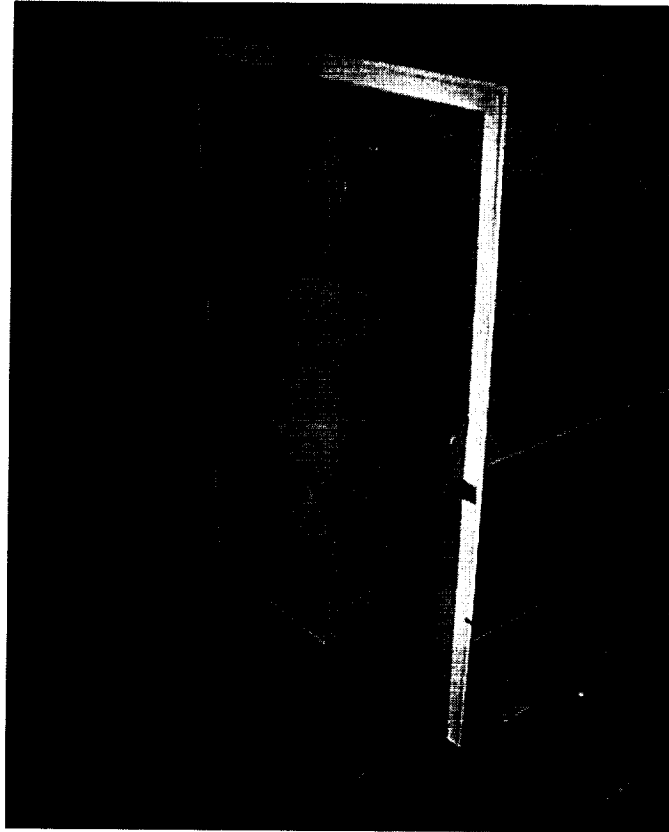
Figure 5: Photograph of boattail plates installed on rear of trailer.
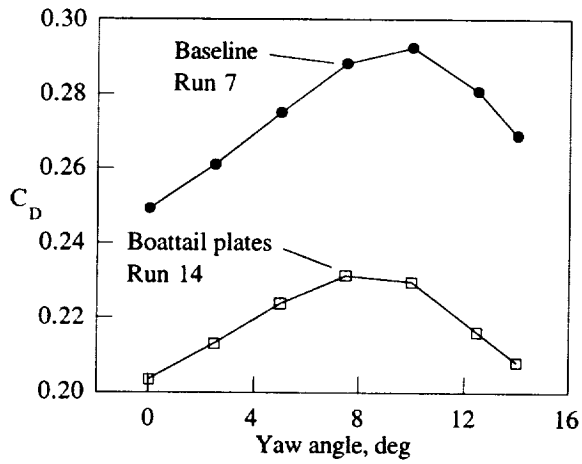
Figure 6: Effect of boattail plates on drag coefficient. Re = 2 million.
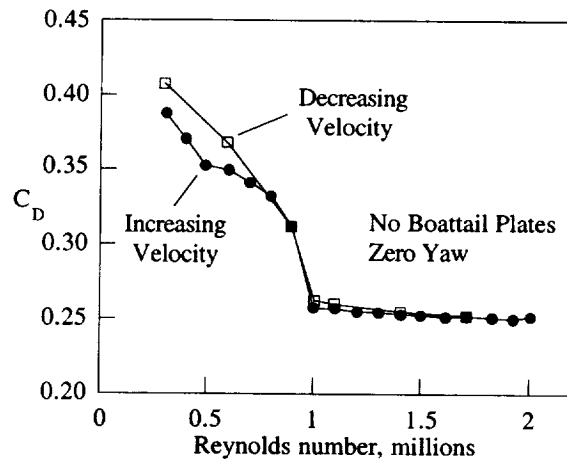
Figure 7: Effect of Reynolds number on baseline drag coefficient.
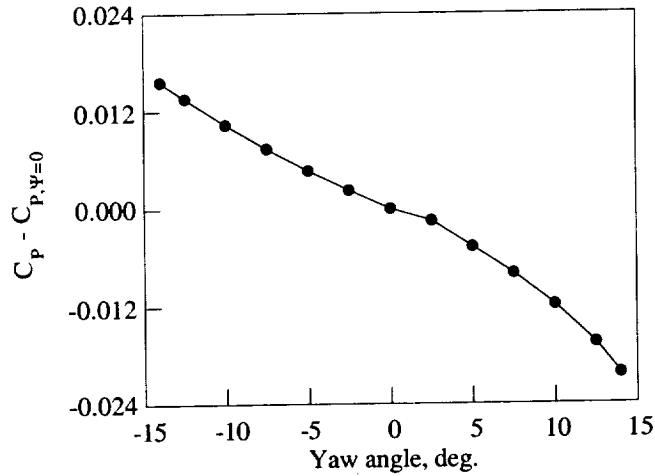
Figure 8: GTS Baseline, Reference wall pressure variation with yaw angle. Pressure coefficients calculated using facility static-pressure ring as static-pressure reference. Re = 2 million.
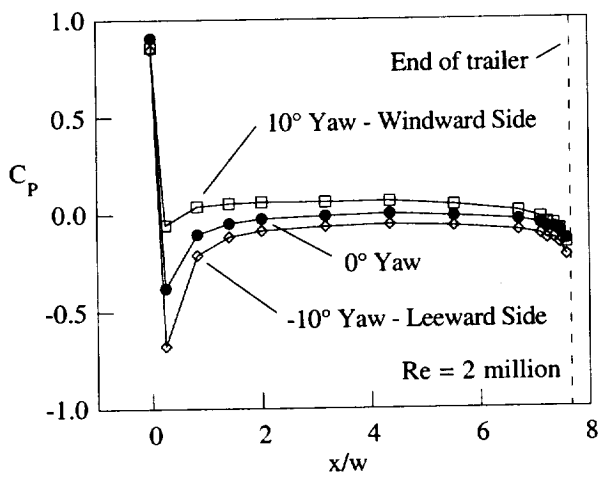
Figure 9: GTS Baseline, Side static-pressure coefficients at y/w = 0.696 (half-height).
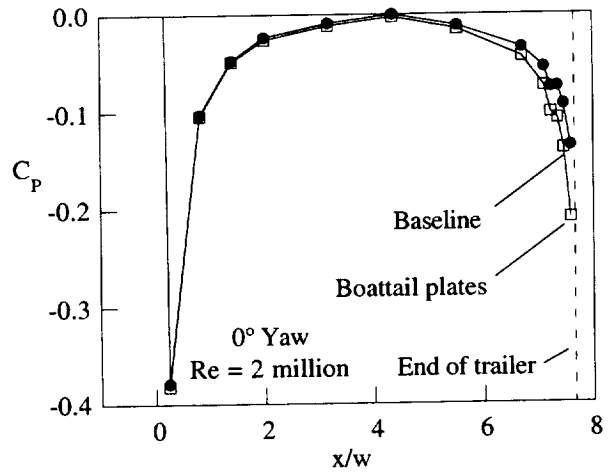
Figure 10: Effect of boattail plates on side static-pressure coefficients.
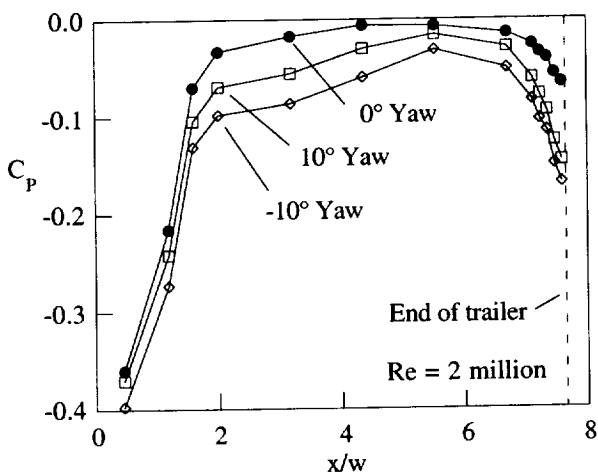
Figure 11: GTS Baseline, Top static-pressure coefficients at z/w = 0.0 (centerline).
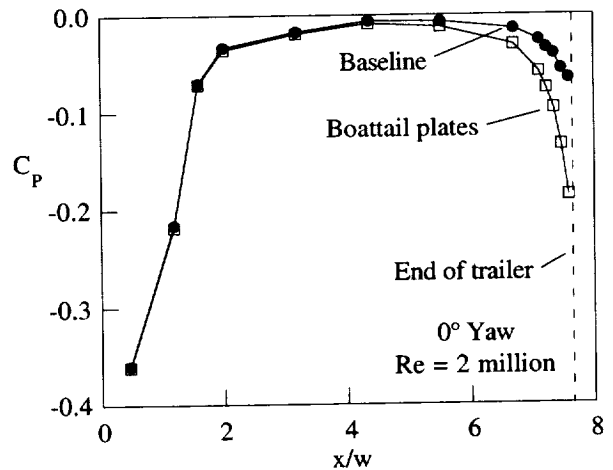
Figure 12: Effect of boattail plates on top static-pressure coefficients.

13
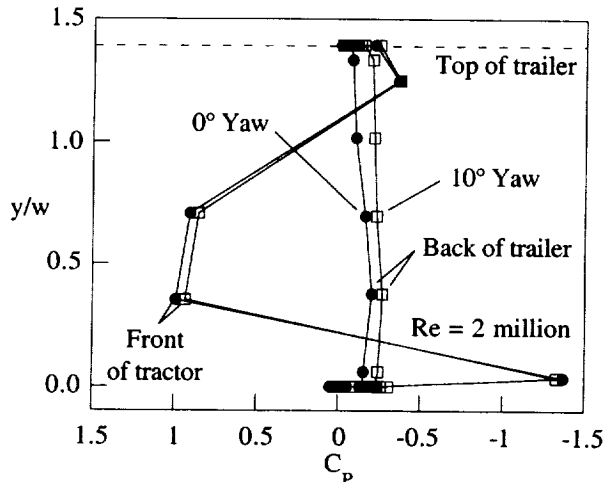
Figure 13: GTS Baseline, Symmetry plane static-pressure coefficients.
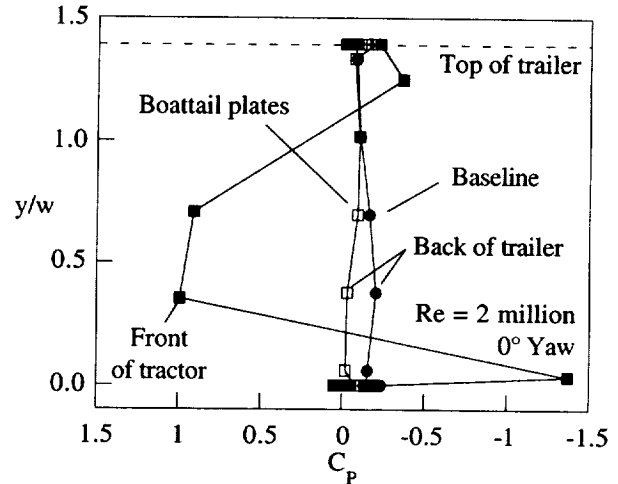
Figure 14: Effect of boattail plates on symmetry plane static-pressure coefficients.
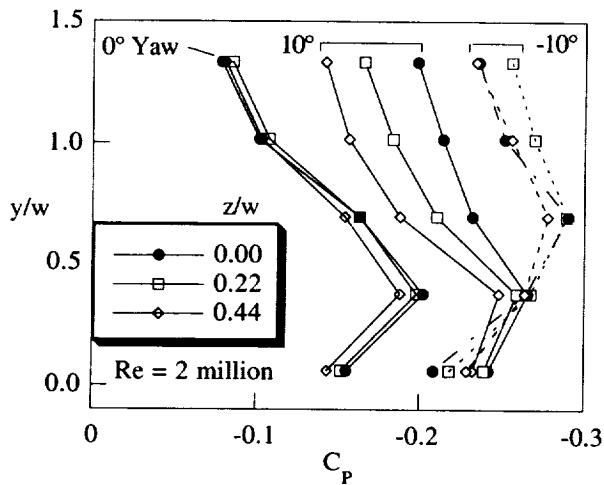
Figure 15: GTS Baseline, Trailer base static-pressure coefficients.
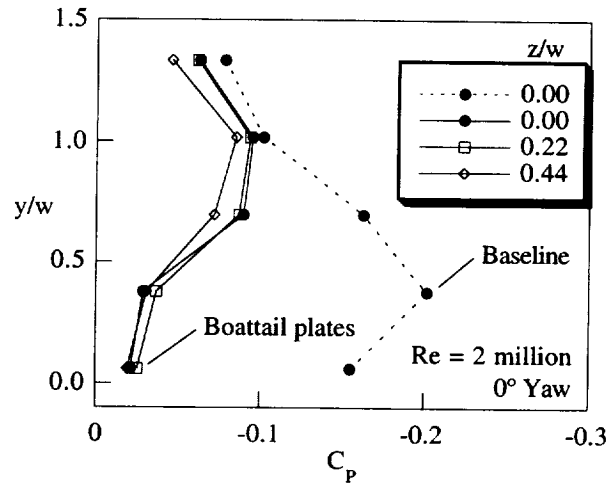
Figure 16: Effect of boattail plates on base static-pressure coefficients.
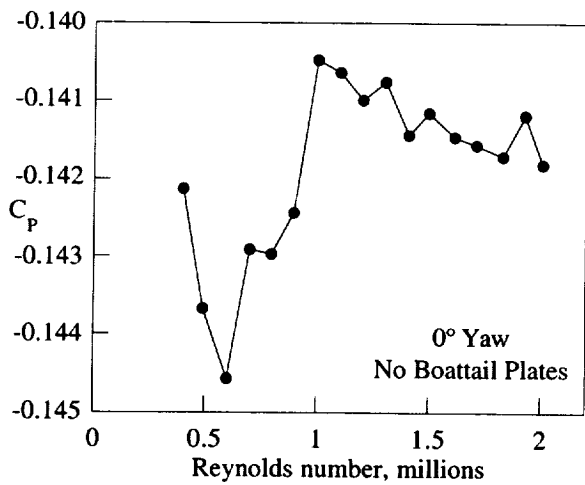
Figure 17: Effect of Reynolds number on the average trailer base pressure at zero yaw.
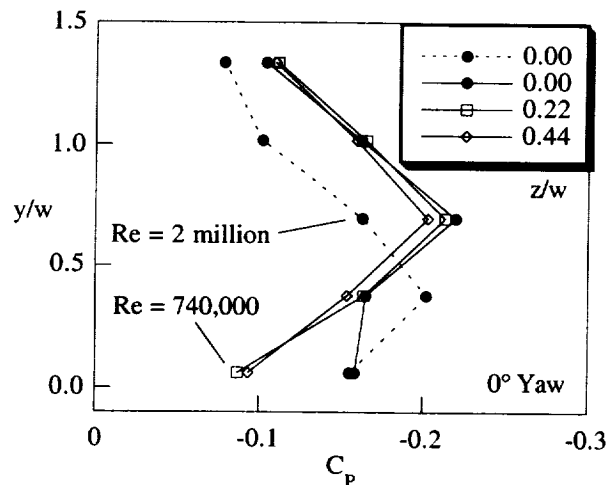
Figure 18: Effect of Reynolds number on the trailer base pressure distribution at zero yaw.

14
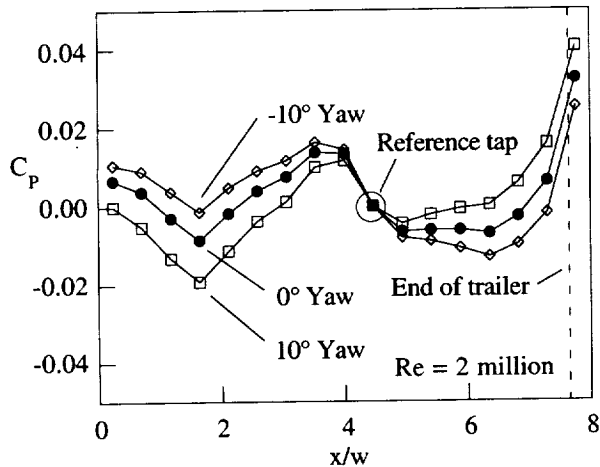
Figure 19: GTS Baseline, Wall pressure coefficients at
y/w = 2.59.
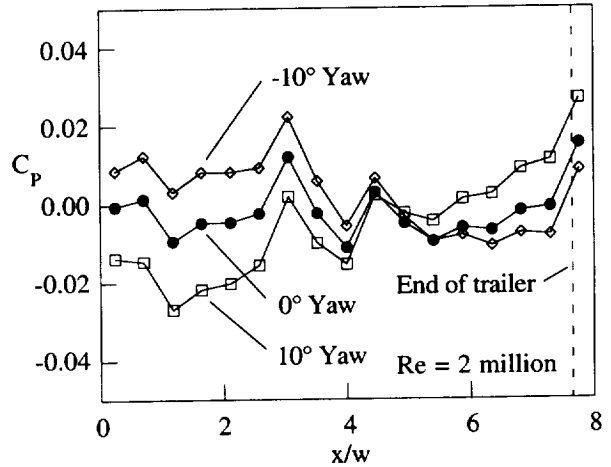
Figure 20: GTS Baseline, Wall pressure coefficients at
y/w = 1.18.
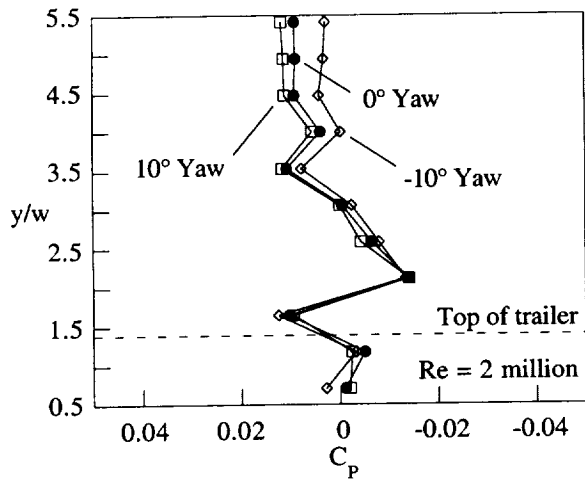
Figure 21: GTS Baseline, Wall pressure coefficients at
x/w = 4.94.
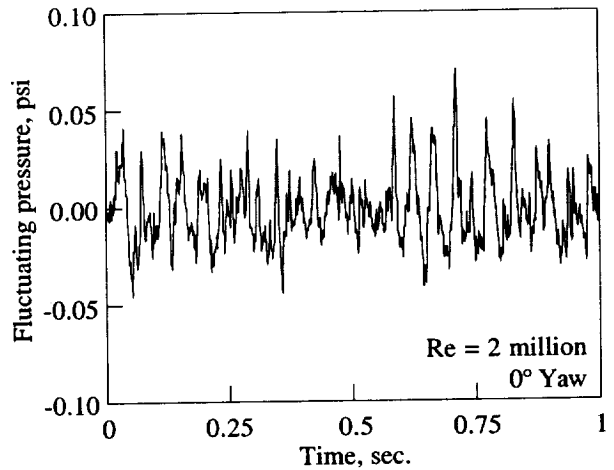
Figure 22: GTS Baseline, Unsteady pressure signal
from sensor on rear of trailer.
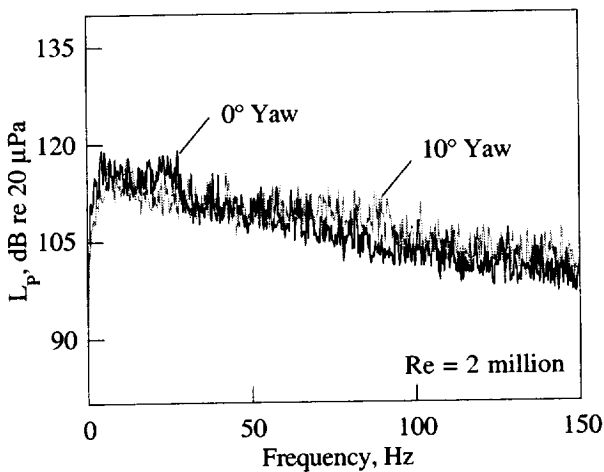
Figure 23: GTS Baseline, Spectra of unsteady pressure
sensor on rear of trailer at Ψ = 10°.
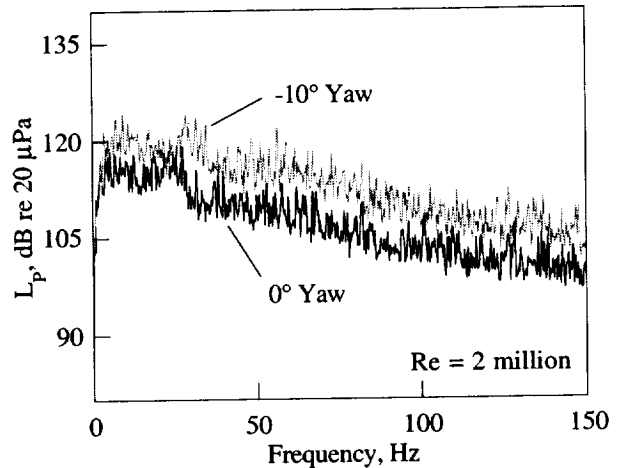
Figure 24: GTS Baseline, Spectra of unsteady pressure
sensor on rear of trailer at Ψ = -10°.
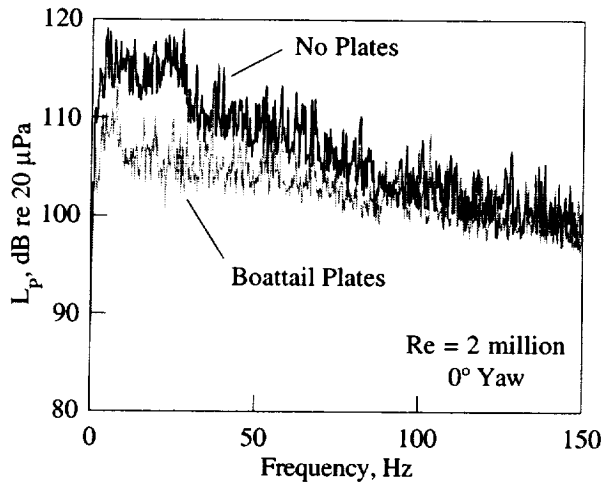
Figure 25: Effect of boattail plates on unsteady pressure spectra.
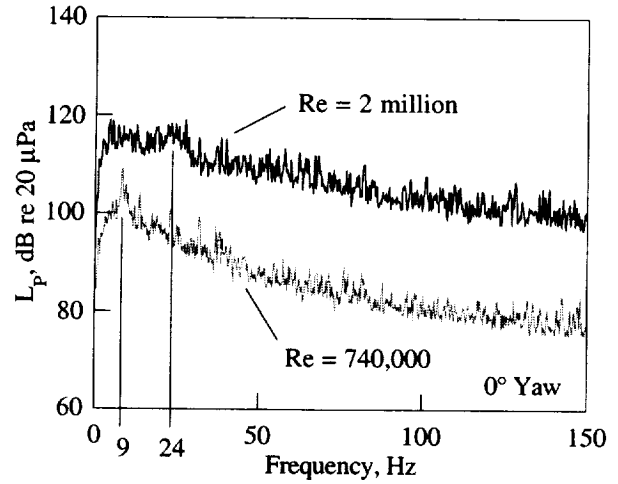
Figure 26: GTS Baseline, Effect of Reynolds number on unsteady pressure spectra.
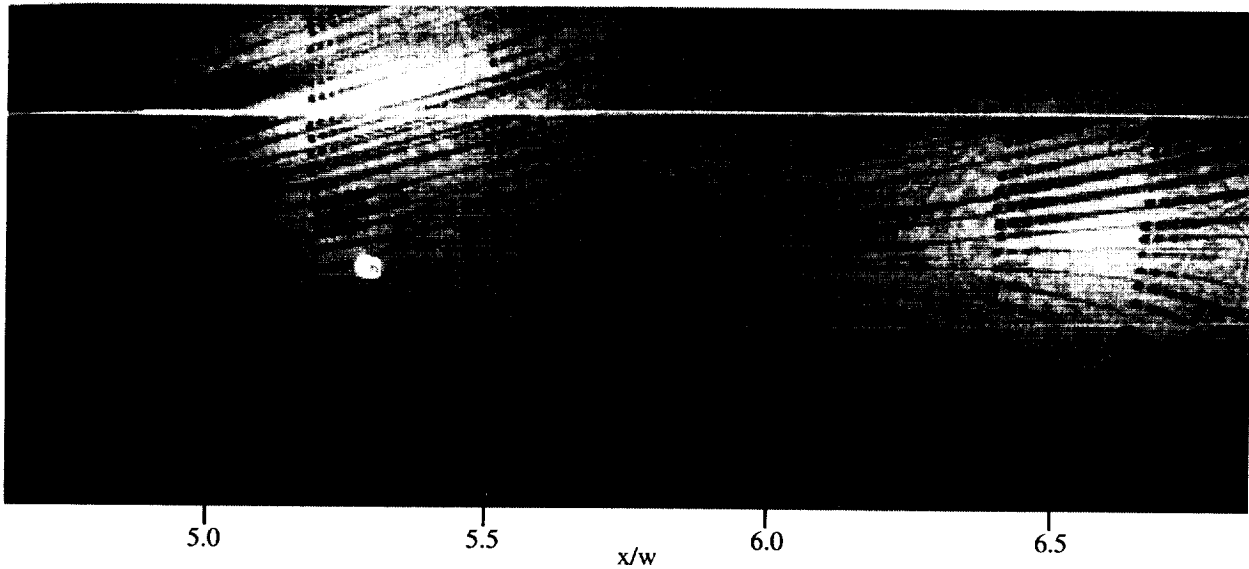
Figure 27: Oil-film interferometry image showing vortex roll-up on top of truck at 10 deg. yaw. Skin friction is proportional to spacing between interference bands. Flow from left to right.
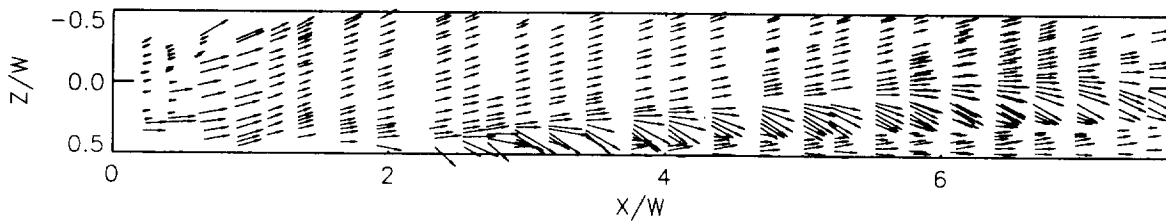
Figure 28: Skin friction vectors on top of the truck from oil-film measurements at 10 deg. yaw. Re = 2 million.

16
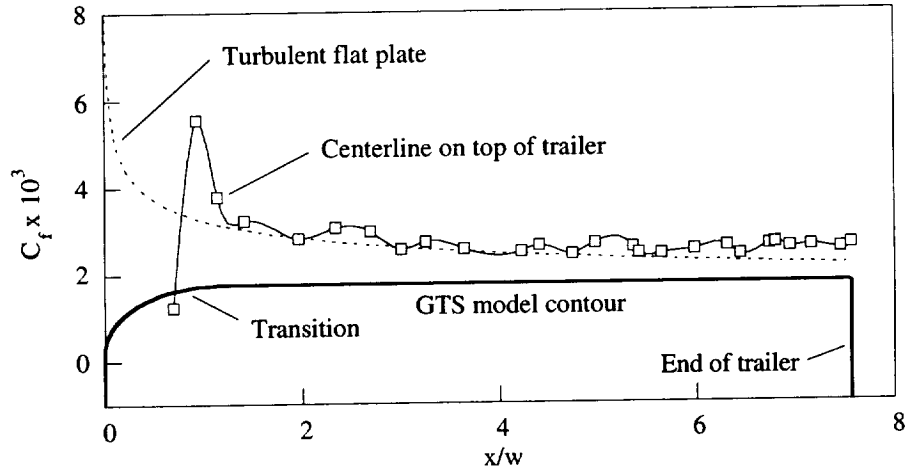
Figure 29: Skin friction coefficients on top of trailer from oil-film interferometry measurements at zero yaw. Re = 2 million.
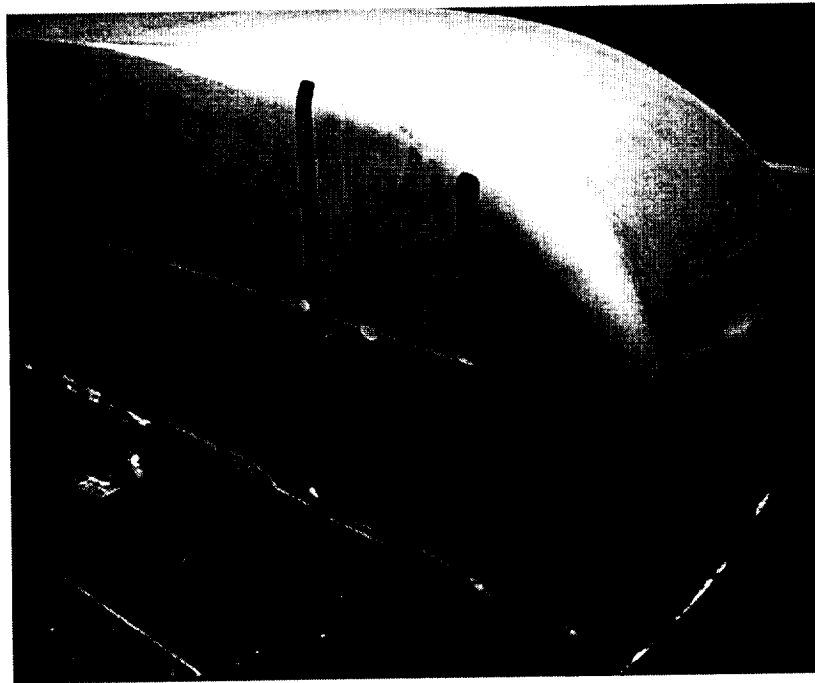
Figure 30: Hot-film sensor sheets mounted on the side of the GTS model.
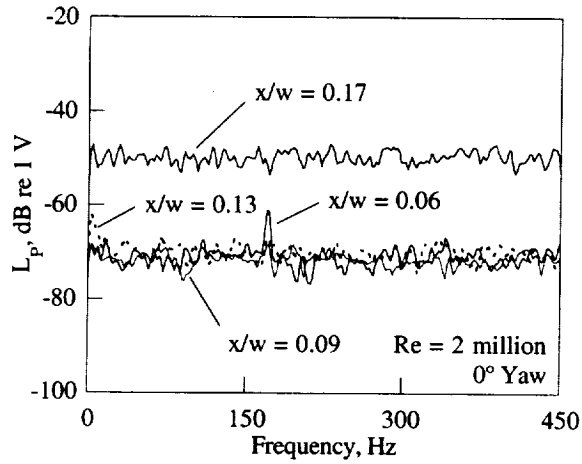
Figure 31: GTS Baseline, Spectra of adjacent hot-film
sensors on the right side of the model at
$\Psi = 0°$(y/w = 0.35).
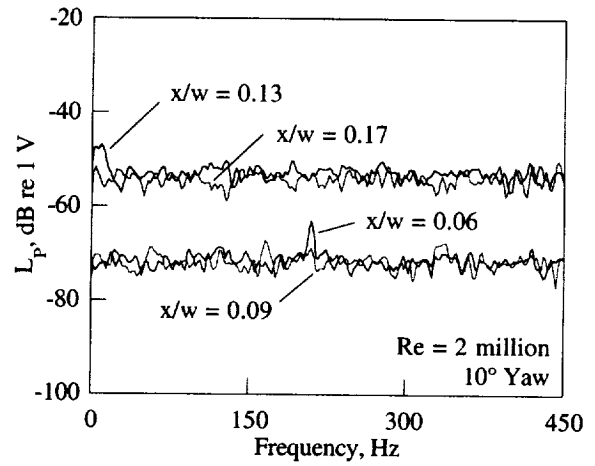
Figure 32: GTS Baseline, Spectra of adjacent hot-film
sensors on the right side of the model at
$\Psi = 10°$(y/w = 0.35).
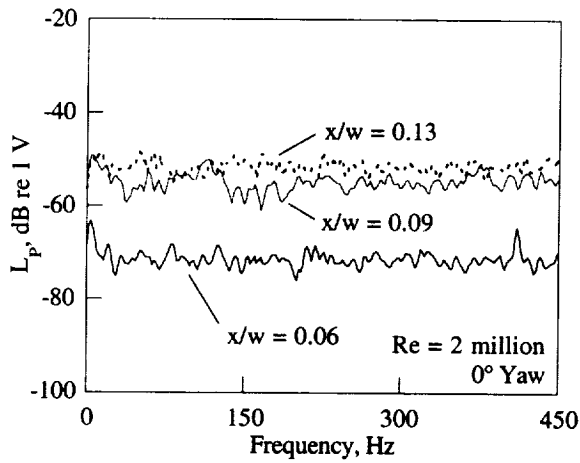
Figure 33: GTS Baseline, Spectra of adjacent hot-film
sensors on the right side of the model at
$\Psi = 10°$(y/w = 0.64).
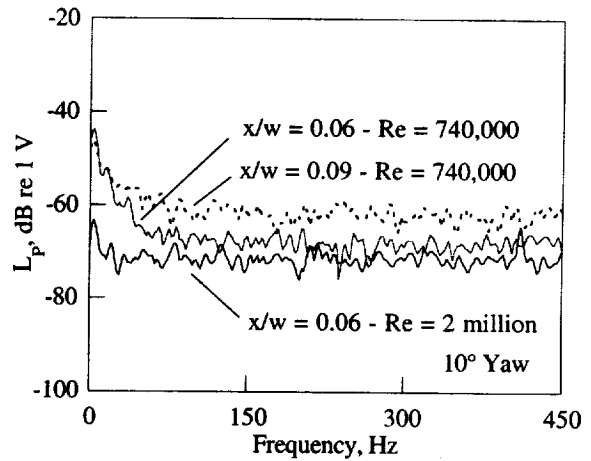
Figure 34: GTS Baseline, Spectra of adjacent hot-film
sensors on the right side of the model at
$\Psi = 10°$(y/w = 0.64)
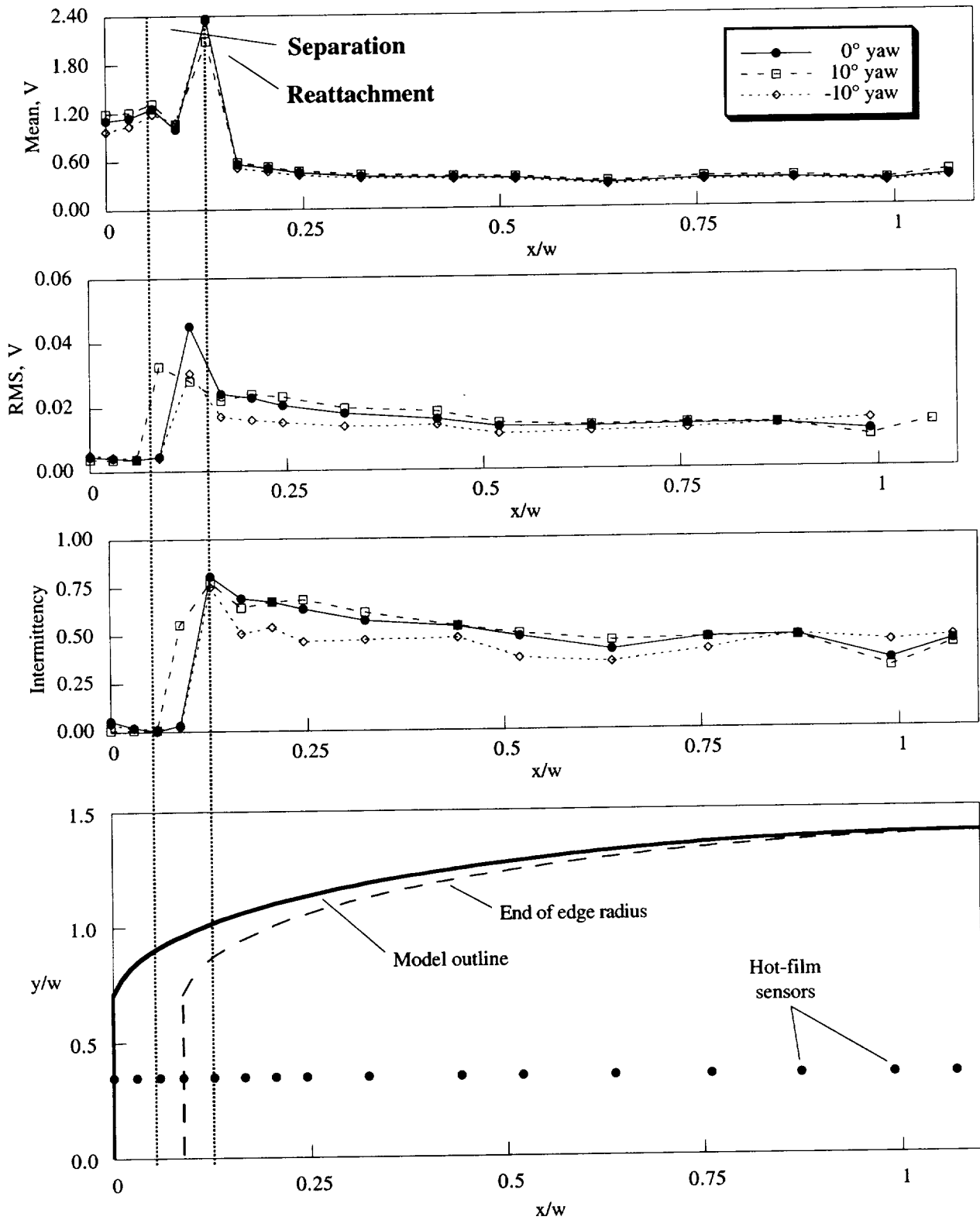
Figure 35: Hot-film measurements on the right side of the truck for yaw = 0, 10, & –10 deg. Flow direction is from left to right. Re = 2 million.

19

Horizontal Plane

Vertical Cross-stream Plane

Flo
w

GTS model

Laser light sheet

Image area
(35 cm x 50.8 cm)

Camera

Vertical Streamwise Plane
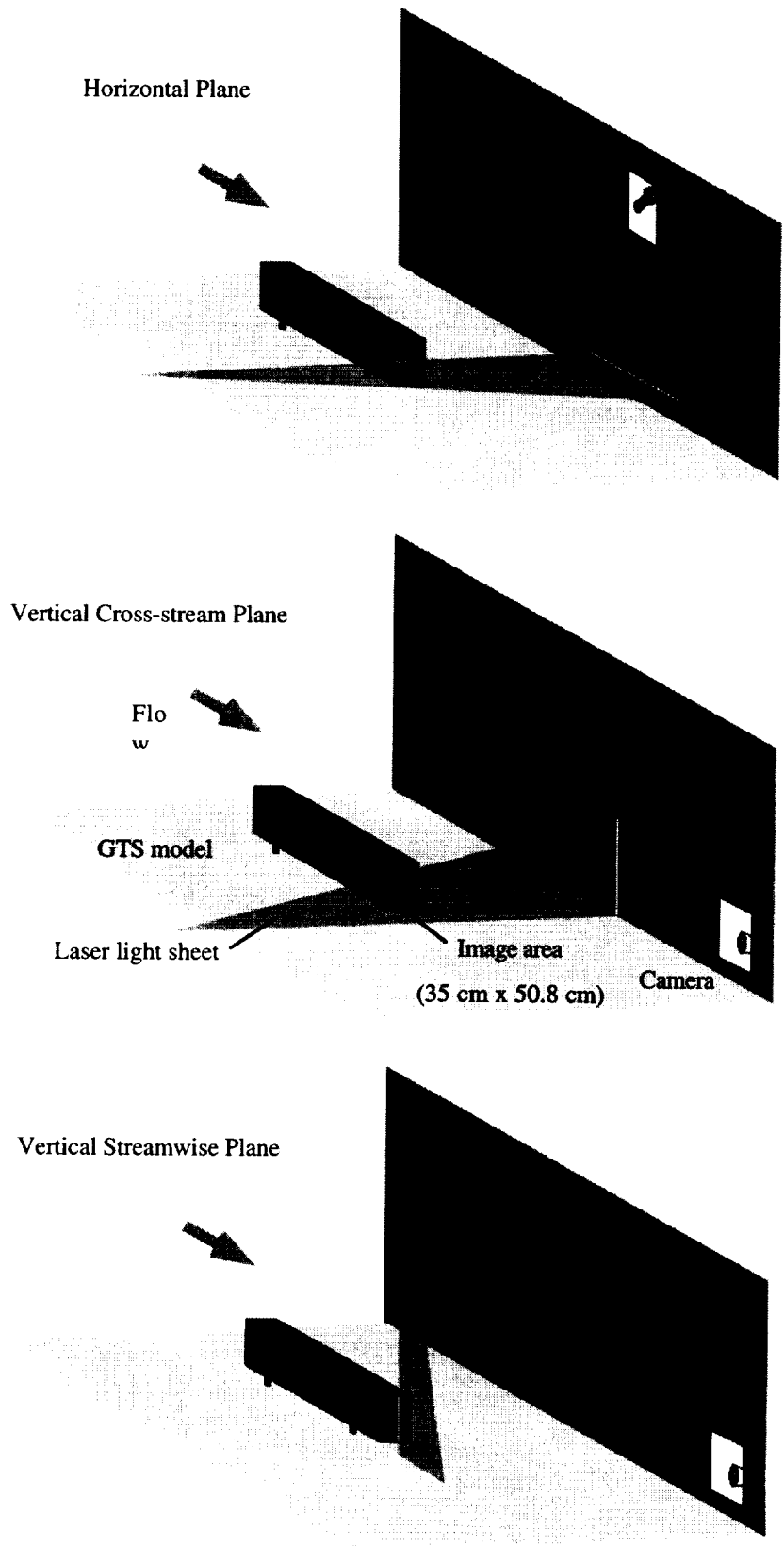
Figure 36: Measurement plane orientations for particle image velocimetry in the trailer wake.
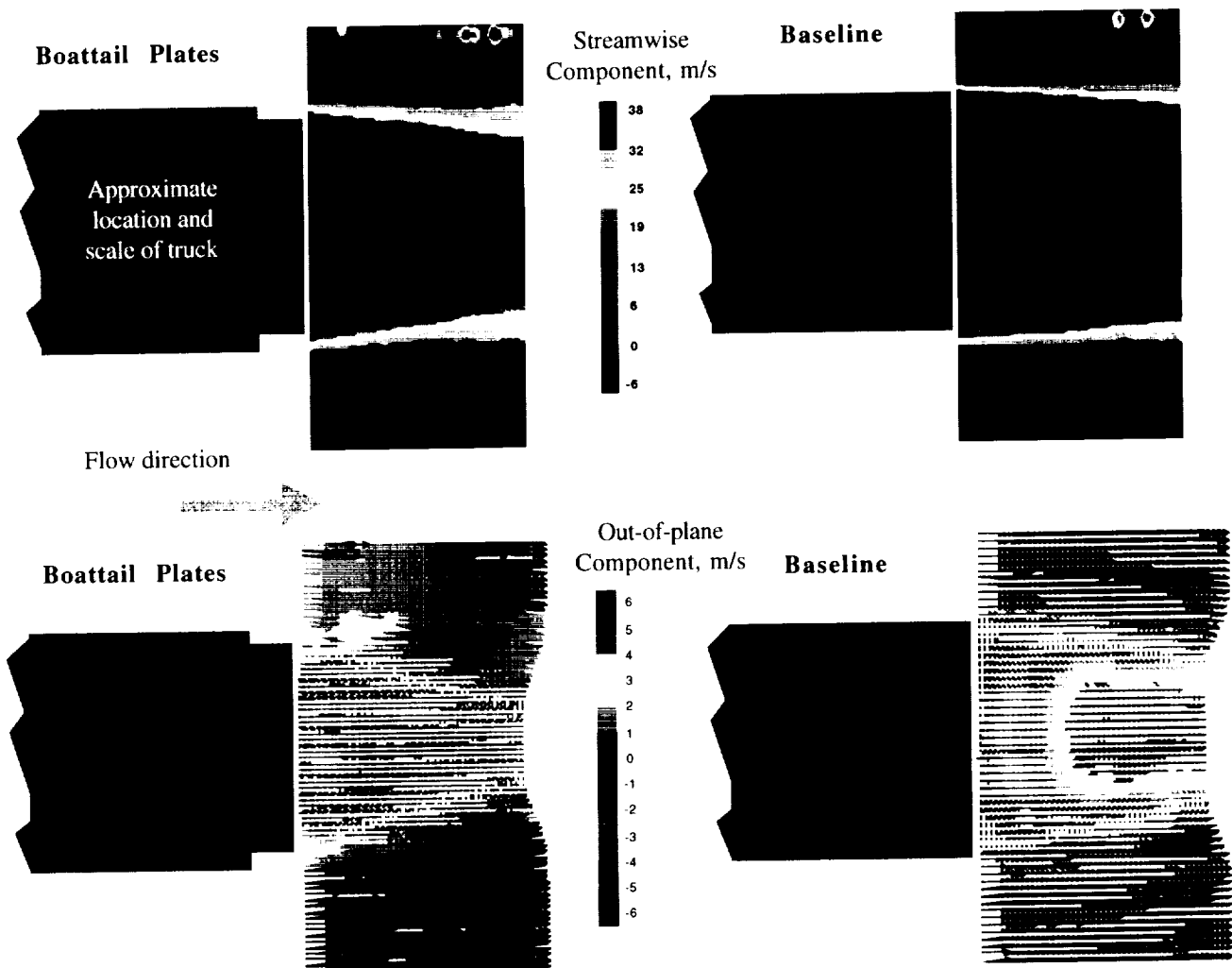
Figure 37: Particle image velocimetry measurements in the wake of the trailer with and without boattail plates. Horizontal plane at half height (y/w = 0.696), time averaged. Re = 2 million.

REPORT DOCUMENTION PAGE

Public reporting burden for this collection of information is estimated to average 1 hour per response, including the time for reviewing instructions, searching existing data sources, gathering and maintaining the data needed, and completing and reviewing the collection of information. Send comments regarding this burden estimate or any other aspect of this collection of information, including suggestions for reducing this burden, to Washington Headquarters Services, Directorate for Information Operations and Reports, 1215 Jefferson Davis Highway, Suite 1204, Arlington, VA 22202-4302, and to the Office of Management and Budget, Paperwork Reduction Project (0704-0188), Washington, DC 20503.

1. AGENCY USE ONLY (Leave blank)	2. REPORT DATE	3. REPORT TYPE AND DATES COVERED
	February 2001	Technical Memorandum

4. TITLE AND SUBTITLE

An Experimental Study of the Ground Transportation System (GTS) Model in the NASA Ames 7- by 10-Ft Wind Tunnel

5. FUNDING NUMBERS

RTOP 522-21-72-52-98

6. AUTHOR(S)

Bruce L. Storms,* James C. Ross, James T. Heineck, Stephen M. Walker, David M. Driver, Gregory G. Zilliac

7. PERFORMING ORGANIZATION NAME(S) AND ADDRESS(ES)

Ames Research Center, Moffett Field, CA 94035-1000 and
*AerospaceComputing, Inc., Los Altos, CA 94022

8. PERFORMING ORGANIZATION REPORT NUMBER

A-00V0031

9. SPONSORING/MONITORING AGENCY NAME(S) AND ADDRESS(ES)

National Aeronautics and Space Administration
Washington, DC 20546-0001 and
U.S. Department of Energy, Washington, DC 20585

10. SPONSORING/MONITORING AGENCY REPORT NUMBER

NASA TM- 2001-209621

11. SUPPLEMENTARY NOTES

Point of Contact: James C. Ross, Ames Research Center, MS 260-1, Moffett Field, CA 94035-1000
(650) 604-6722

12a. DISTRIBUTION/AVAILABILITY STATEMENT

Unclassified—Unlimited   Distribution: Standard
Subject Category – 02
Availability: NASA CASI (301) 621-0390

12b. DISTRIBUTION CODE

13. ABSTRACT (Maximum 200 words)

The 1/8-scale Ground Transportation System (GTS) model was studied experimentally in the NASA Ames 7- by 10-Ft Wind Tunnel. Designed for validation of computational fluid dynamics (CFD), the GTS model has a simplified geometry with a cab-over-engine design and no tractor-trailer gap. As a further simplification, all measurements of the GTS model were made without wheels. Aerodynamic boattail plates were also tested on the rear of the trailer to provide a simple geometry modification for computation. The experimental measurements include body-axis drag, surface pressures, surface hot-film anemometry, oil-film interferometry, and 3-D particle image velocimetry (PIV). The wind-averaged drag coefficient with and without boattail plates was 0.225 and 0.277, respectively. PIV measurements behind the model reveal a significant reduction in the wake size due to the flow turning provided by the boattail plates. Hot-film measurements on the side of the cab indicate laminar separation with turbulent reattachment within 0.08 trailer width for zero and ±10 degrees yaw. Oil film interferometry provided quantitative measurements of skin friction and qualitative oil flow images. A complete set of the experimental data and the surface definition of the model are included on a CD-ROM for further analysis and comparison.

14. SUBJECT TERMS

Bluff Body Aerodynamics, Truck Drag, GTS Model

15. NUMBER OF PAGES

24

16. PRICE CODE

A03

17. SECURITY CLASSIFICATION OF REPORT	18. SECURITY CLASSIFICATION OF THIS PAGE	19. SECURITY CLASSIFICATION OF ABSTRACT	20. LIMITATION OF ABSTRACT
Unclassified	Unclassified		

NSN 7540-01-280-5500